Research Article | Vol. 26, No. 16 | 6 Aug 2018 | OPTICS EXPRESS 20211
Optics EXPRESS

Geometric frustration in a hexagonal lattice of plasmonic nanoelements

ANA CONDE-RUBIO,[1,2] ARANTXA FRAILE RODRÍGUEZ,[1,2] XAVIER BORRISÉ,[3] FRANCESC PEREZ-MURANO,[4] XAVIER BATLLE[1,2] AND AMÍLCAR LABARTA[1,2,*]

[1] *Departament de Física de la Matèria Condensada, Universitat de Barcelona, Barcelona, 08028, Spain*
[2] *Institut de Nanociència i Nanotecnologia, Universitat de Barcelona (IN2UB), Barcelona, 08028, Spain*
[3] *Catalan Institute of Nanoscience and Nanotechnology (ICN2), CSIC and The Barcelona Institute of Science and Technology, Campus UAB, Bellaterra, 08193 Barcelona, Spain*
[4] *Institut de Microelectrónica de Barcelona (IMB-CNM, CSIC), Bellaterra, 08193, Spain*
*amilcar.labarta@ub.edu

Abstract: We introduce the concept of geometric frustration in plasmonic arrays of nanoelements. In particular, we present the case of a hexagonal lattice of Au nanoasterisks arranged so that the gaps between neighboring elements are small and lead to a strong near-field dipolar coupling. Besides, far-field interactions yield higher-order collective modes around the visible region that follow the translational symmetry of the lattice. However, dipolar excitations of the gaps in the hexagonal array are geometrically frustrated for interactions beyond nearest neighbors, yielding the destabilization of the low energy modes in the near infrared. This in turn results in a slow dynamics of the optical response and a complex interplay between localized and collective modes, a behavior that shares features with geometrically frustrated magnetic systems.

1. Introduction

Plasmonic nanoelement arrays have been widely used for a variety of applications including enhanced spectroscopies [1–5], perfect absorbers [6–8], plasmonic lasing [9–11] or energy harvesting [12]. Innumerable research has been done in fully characterizing the spectral response or the field enhancement (FE) of a variety of nanoantennas [2,4,13–16]. Besides, many studies have analyzed the response of nanoparticle arrays where interparticle interactions are significant [11,14–22]. In these systems, when the interparticle separation is of the order of the resonance wavelength, far-field interactions between the nanoelements in the array may result in constructive interferences giving rise to collective modes known as Surface Lattice Resonances (SLR). In this case, each element in the array is excited not only by the impinging radiation but also by the light scattered by other nanoelements, yielding a collective coupling among all of them. Moreover, the optical response of the system may also be governed by the near-field coupling between nearest neighbors giving rise to Localized Surface Resonances (LSR). Whereas LSR usually exhibit broad extinction peaks due to radiative damping, SLR present sharp linewidths that could be more suitable for applications profiting from a high frequency specificity [21–25]. Interestingly, for incoming radiation around normal incidence and with a wavelength matching one of the diffraction edges of the Bravais lattice of the array, a SLR mode due to the lattice diffraction shows up. This mode may interfere with one of the LSR modes, resulting in a sharp asymmetric dip superimposed to the LSR peak of the extinction spectrum that corresponds to a kind of Fano resonance [14,18].

The effect that the symmetry of the array has on the plasmonic response, and in particular, on the occurrence of SLR and Fano resonances, has been studied in a number of different lattices [17–19]. At normal incident radiation, slight differences in the spectra have been observed as a function of lattice geometries for the same diffraction edge [19], and only for oblique incident light those differences became more noticeable [17]. This brings up the question whether it is possible to take advantage of the delocalized nature of

#332491 https://doi.org/10.1364/OE.26.020211
Journal © 2018 Received 23 May 2018; revised 29 Jun 2018; accepted 10 Jul 2018; published 25 Jul 2018

Optics EXPRESS

the SLR to explore excitation modes beyond nearest-neighbor interactions in lattices where interacting electric dipoles are topologically frustrated. The main goal would be the excitation of a variety of coupled modes with slow decaying times, which might share features with those kinds of excitations taking place in geometrically frustrated magnetic systems such as spin ices [26,27]. In particular, honeycomb lattices of nanoparticles have been studied due to its similarity with graphene, expecting to mimic some of its unique properties [17,20,28]. For example, the theoretical work by Mariani and Weick proved that honeycomb arrays of small metallic nanoparticles could exhibit collective plasmon modes similar to electrons in graphene, opening up the possibility for high tunability and control of the light propagation and subwavelength lateral confinement in plasmonic metamaterials [28]. Thus, several experimental studies have been carried out on honeycomb lattices [17–20]. However, none of them have showed any remarkable effects related to the geometrical frustration of dipolar interactions.

Moreover, SLR modes have been studied in systems where magnetic and plasmonic materials are combined to tune their magneto-optical activity [23,29–31]. In fact, the combination of near-field and far-field interactions was proven to be very efficient to use magneto-plasmonic nanodisks for refractive index sensing [23].

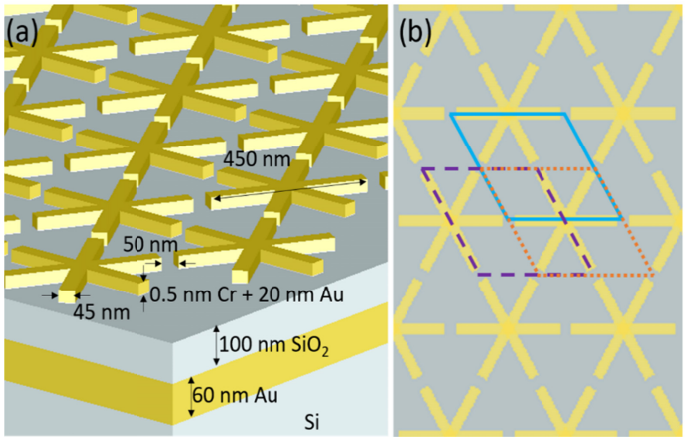

Fig. 1. (a) Scheme of the fabricated nanostructures in the MIM configuration. (b) Unit cells of the three interpenetrated hexagonal lattices of nanogaps.

In this article, we present the fabrication, the optical characterization and the numerical simulations of arrays of asterisk-shaped Au nanoelements arranged in a hexagonal lattice with a pitch of the order of the resonance frequency so that SLR modes may occur in the optical spectral range [Fig. 1(a)], showing almost perfect absorption. The six rectangular thin bars that make up every asterisk leave small gaps between nearest-neighbor elements of only tens of nanometers in width [Fig. 1(a)] allowing for strong near-field coupling between them. Thus, the lowest energy excitation modes (LSR modes) of the array will be associated with strong dipolar polarization of pairs of facing bars forming the gaps. However, the whole array of gaps can be viewed as three interpenetrated hexagonal lattices [Fig. 1(b)] due to the three possible spatial orientations of the gaps in the array. These three lattices are geometrically frustrated when the gaps are excited as localized dipoles and interactions beyond nearest neighbors are considered [32]. Consequently, this frustration destabilizes the LSR modes, favoring the excitation of delocalized higher energy modes (SLR modes) that exchange energy with the LSR modes. A thorough numerical study of the optical response of the system shows a slow decaying time of the optical response evolving in a pseudo-periodic manner through a variety of excitation modes resulting from different combinations of the two following basic modes: (i) a LSR mode enhancing the electric field within the gaps, which is compatible with the linear polarization of the excitation pulse; and (ii) a SLR collective mode of the asterisk-shaped nanoelements minimizing the electric field within the gaps

Optics EXPRESS

and being compatible with the translational symmetry of the hexagonal lattice of nanoelements.

2. Results and discussion

2.1 Sample fabrication

Arrays of asterisk-shaped Au nanostructures of 200 μm x 200 μm in total area have been fabricated by means of Electron Beam Lithography (EBL) in a metal-insulator-metal (MIM) configuration. MIM configurations are conventionally used in metamaterial absorbers or Surface Enhanced Infrared Absorption (SEIRA) applications to maximize light absorption [4,16,18]. There are two different approaches for the MIM configuration: (i) the near-field coupling scheme, where the thickness of the dielectric spacer layer is much smaller than the incident light wavelength λ; and (ii) the far-field coupling scheme, based on the Salisbury screen [33], where the thickness of the spacer layer is about $n\lambda/4$, being n the refractive index of the spacer material. In this case, destructive interference is obtained so that there is a total reflection of the incoming light [7]. The latter configuration has been adopted in our samples.

In order to form the MIM stack [Fig. 1(a)], a 60 nm thick Au layer was deposited by electron beam evaporation on a conventional Si wafer, using a 5 nm Ti layer to promote adhesion, followed by the deposition of SiO_2 by Plasma Enhanced Chemical Vapor Deposition (PECVD). The thickness of the spacer layer has been chosen so that total reflection takes place at a wavelength around the SLR peak to enhance collective excitations. The SiO_2 deposition took place in two steps. First, a thin layer was deposited at 50 W of radio frequency (RF) power at 350 °C for 20 seconds, to obtain a thickness of around 20 nm. This layer, which typically accounts for 10-20% of the final total thickness of the SiO_2 layer, serves as a protection for the underlying Au layer. Then, a second deposition took place at a power of 200 W and at a temperature of 380 °C.

Then, poly(methyl methacrylate) (950 PMMA A2, MicroChem) was spin-coated at 1200 rpm for 1 minute onto the substrate and cured at 180 °C for 1 minute. The EBL exposure was done at 20 kV with a 20 μm gun aperture and a step size of 10 nm. The dose was fixed to 180 $\mu A/cm^2$ and the dose factor was changed from area to area to finely tune the size. After the exposure, the sample was developed by dipping it in a 1:3 solution of methyl isobutyl ketone (MIBK) in isopropanol (IPA) for 30 seconds and then rinsed in IPA for 30 seconds to stop the reaction. Then, samples were metallized by electron beam evaporation (ATC Orion, AJA International, Inc). For all samples, a thin (0.5-2 nm) layer of either Ti or Cr was deposited to promote adhesion before growing the Au layer (20-30 nm). Finally, the sample was immersed in acetone at 40 °C for 5 minutes to soften the resist and then ultrasounds were applied to perform the lift-off.

A schematic plot of the samples is shown in Fig. 1(a). Several geometries ranging from asterisk- [Fig. 2(a)] to star-shaped [Fig. 2(d)] nanoelements were prepared. Besides, the pitch of the array and the gap size were varied from 400 to 500 nm and from 20 to 100 nm, respectively.

Optics EXPRESS

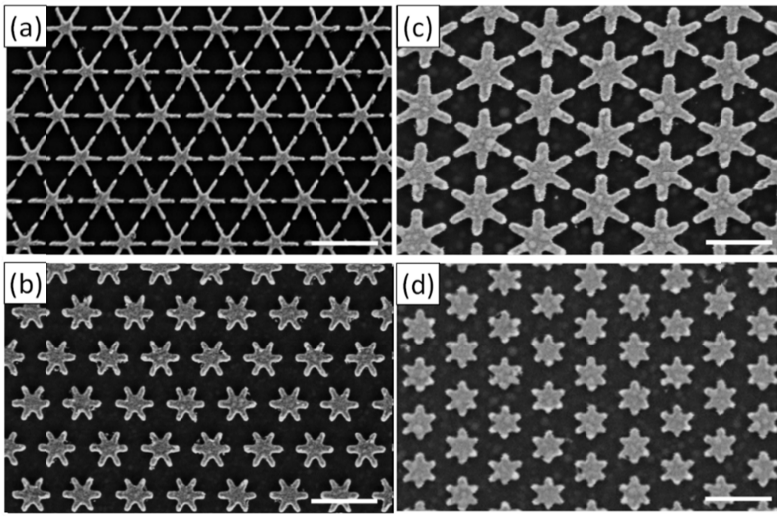

Fig. 2. Representative SEM micrographs corresponding to different samples, from asterisk- (a) to star-shaped (d) nanoelements, obtained by changing the fabrication parameters. Scale bars: 500 nm.

2.2. FTIR spectroscopy

To study the plasmonic response of the nanostructures, Fourier Transform Infrared Spectroscopy (FTIR) (Vertex 70 and Hyperion, Bruker) was used in reflection configuration with unpolarized light and a 4x objective. During the experiments, knife-edge apertures were set to measure the whole EBL patterned area and a Ag mirror was used as background.

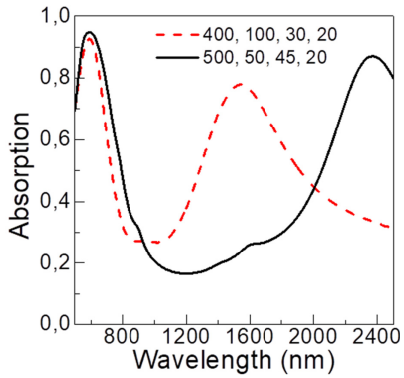

Fig. 3. Absorption spectra measured by FTIR in reflection configuration for two arrays in MIM configuration, being the SiO_2 thickness 100 nm: 400 nm / 100 nm / 30 nm / 20 nm (red dashed line) and 500 nm / 50 nm / 45 nm / 20 nm (black solid line) (pitch / gap / width / thickness), corresponding to the SEM micrographs shown in Fig. 2(b) and 2(c), respectively.

Figure 3 shows the absorption spectra measured in reflection. The absorption (A) was calculated as A = 1-R-T after measuring the reflection spectrum (R) and assuming that the transmission (T) is equal to 0, since the thickness of the deposited Au mirror film is large enough to prevent the light from passing through. In particular, results for the two cases in Fig. 2 with a 100 nm-thick SiO_2 layer are shown: the black solid line corresponds to a 500 nm pitch sample with 50 nm wide gaps and 45 nm wide bars, and the red dashed one to an array with a 400 nm pitch with 100 nm wide gaps and 30 nm wide bars. The spectra show two high absorption peaks, one in the visible region (VIS) and the other in the near infrared region (NIR) of the electromagnetic spectrum. Remarkable absorption efficiency over 90% is found in the visible range for pitch values of 400 and 500 nm. In

Optics EXPRESS

addition, the location of the VIS peak is almost insensitive to changes in the geometrical parameters of both the nanoelement and the array, in contrast to the NIR peak which shows a strong dependence.

2.3. FDTD simulations

For a better understanding of the plasmonic response of the arrays, Finite-Difference Time Domain (FDTD) simulations using the Lumerical FDTD Solutions package [34] were carried out to calculate the absorption spectrum, the near-field intensity, the charge distribution, and the time evolution of the optical response.

The refractive indices were taken from the data set included in Lumerical's database and correspond to the data from Palik [35] for the case of Cr, Ti, Si and SiO_2 and Johnson's and Christy [36] data for the case of Au. The background dielectric constant was taken to be 1. The array was excited by an incident pulse normal to the plane containing the system, and the electric field was parallel to the *x*-axis. Symmetric and antisymmetric conditions were used in the *x*- and *y*-axes to simulate only one quarter of unit cell and minimize the computing time. Perfectly matched layer (PML) boundaries were used in the *z*-axis. Simulations of a single element were also performed using a Total-Field Scattered-Field source and two detector boxes placed outside and inside the source to measure the scattering and absorption cross-sections, respectively.

It has been shown that, in most cases, the Ti or Cr layers used to promote adhesion of Au may yield critical effects on the optical response producing a strong weakening of it [4,37,38]. Therefore, all the simulations include a 0.5 nm-thick Cr layer under the Au nanostructures to make them comparable to the fabricated samples. Figure 4 shows the response of a single asterisk and an array of 500 nm / 50 nm / 45 nm / 30 nm (pitch / gap / width / thickness) asterisk-shaped nanoelements.

Although the fabricated samples were metallized with a 20 nm-thick Au layer, the simulations were performed for 30 nm-thick Au which optimizes the absorption (see Appendix for further information). We did not succeed in manufacturing samples with 30 nm-thick Au layer due to some issues in the lift-off process. The absorption spectra, calculated with and without the MIM configuration, are shown in Fig. 4(b), which also shows that transmitted light in the MIM configuration is negligible. In the former, a 100 nm-thick SiO_2 layer was used as a spacer [Fig. 1(a)]. The absorption of the system is clearly higher in MIM configuration [Fig. 4(b)], whose spectrum exhibits two intense peaks, one wide NIR peak (2277 nm) and a narrow one slightly above the visible region (764 nm). The latter displays a quality factor of 19 and reaches 98.4% of absorbance, making these structures nearly-perfect absorbers. Besides, a less intense but also sharp peak is located at 624 nm, which is only present in MIM configuration.

Simulations show a slight change in the location of the high-order energy peak as a function of pitch, gap width or length of the bars, while the wavelength of the NIR peak is strongly dependent on those parameters (see Appendix), in good agreement with the experimental data shown in Fig. 3. However, the VIS peak in the FTIR measurements [Fig. 3] is much broader than in the simulations. This difference may be attributed to several factors, such as the imperfections at the interfaces between both the substrate and the Cr layer, and the Cr and Au layers, or the variability in the shape of the nanoelements due to imperfections in the fabrication process. The latter gives rise to a width distribution of the gaps, roughness and rounded edges of the fabricated nanoelements [Fig. 2], as compared to the ideal asterisk-shaped nanostructures used in the simulations (see Appendix for further information). Moreover, the secondary VIS peak at 624 nm observed in the simulation in MIM configuration is likely merged into the high-order broad peak of the experimental data.

Optics EXPRESS

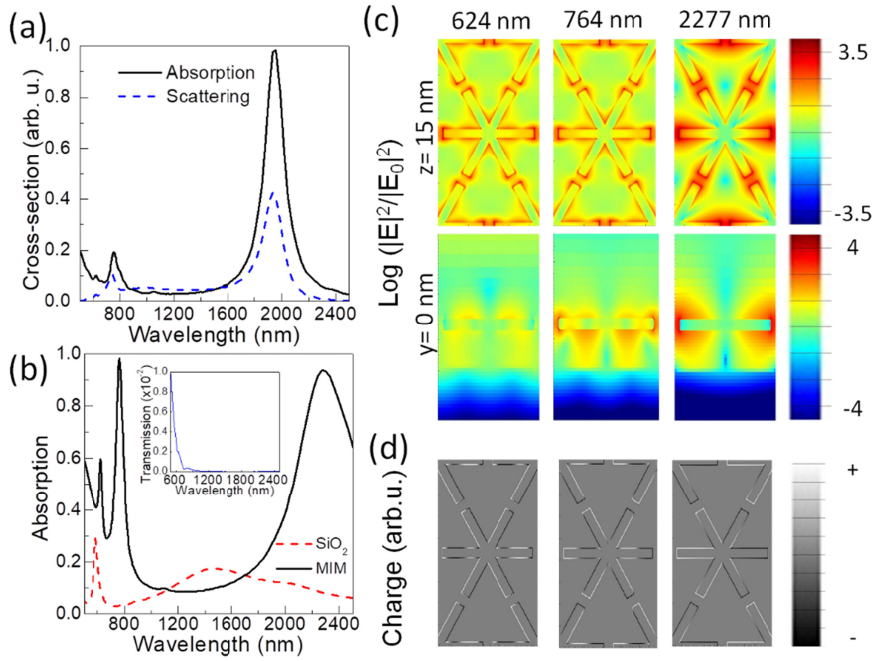

Fig. 4. FDTD simulations of (a) a single Au nanoasterisk of 450 nm / 45 nm / 30 nm (length / width /thickness) in MIM configuration with a 100 nm thick SiO_2 layer and (b) an array of 500 nm / 50 nm / 45 nm / 30 nm (pitch / gap / width / thickness) asterisk-shaped Au nanostructures in MIM configuration with a 100 nm thick SiO_2 layer (black solid line), and on a SiO_2 substrate (red dashed line), the inset showing the transmission for the MIM substrate. Both cases have an incident radiation perpendicular to the *xy* plane and with the electric field parallel to the *x*-axis. (c) *Log* $(|E|^2/|E_0|^2)$ for z = 15 nm (upper row), and y = 0 nm (bottom row) planes (these planes are referred to an arbitrary origin located on top of the SiO_2 spacer layer under the center of one of the nanoelements, being the *x*-axis parallel to the electric field of the incident radiation) and (d) charge distributions, at 624 nm (left), 764 nm (center), and 2277 nm (right) for the array in (b).

The spatial distributions of the relative Field Enhancement (FE = $|E|^2/|E_0|^2$) in logarithmic scale, *log* $(|E|^2/|E_0|^2)$, corresponding to the wavelengths of the three peaks in the simulated absorption spectrum, are shown in Fig. 4(c). The first two rows of panels in Fig. 4(c) show the field distributions for the z = 15 nm and y = 0 planes, respectively, at the wavelengths of maximum absorbance at 624, 764 and 2277 nm [Fig. 4(b)]. For the NIR peak, the electric field is namely concentrated in the gaps and at the end edges of the asterisk bars, resulting in localized LSR modes. In contrast, for the VIS peaks, a more spatially extended electric field enhancement throughout the array is found, mostly in between the tilted bars of each asterisk, giving rise to more complex, collective SLR modes. This kind of SLR excitation is particularly favored by the coupling with the underlying Au film that creates resonances perpendicular to the MIM structure. The charge distributions for the above three absorption peaks are depicted in the corresponding panels in Fig. 4(d), where the major dipolar character of the NIR peak is evidenced, in contrast to the multipolar charge distribution associated with the high-energy modes. The preferential dipolar character of the excitation of the gaps in the NIR peak accounts for its high tunability with the gap width, since as the latter is reduced/increased, the energy of the excitation decreases/increases and accordingly, the NIR peak shifts towards longer/shorter wavelength values (see the relative shifts of the NIR peak in Fig. 3 and Appendix).

Optics EXPRESS

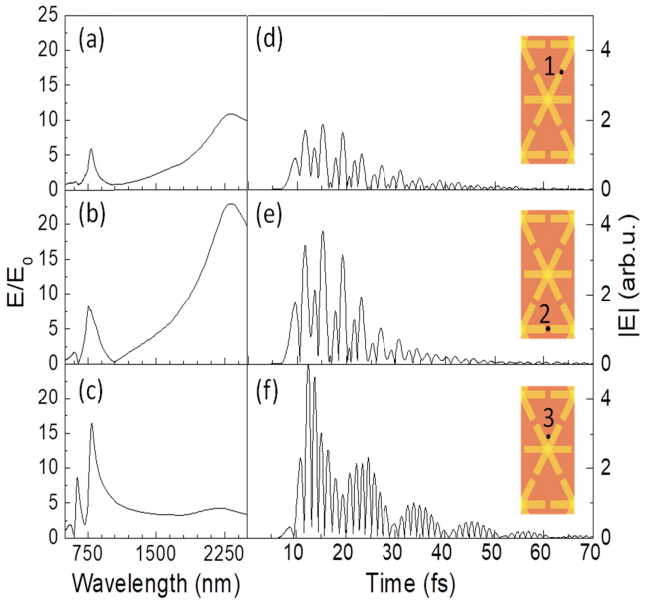

Fig. 5. Time evolution of the optical response of an array of 500 nm / 50 nm / 45 nm / 30 nm (pitch / gap / width / thickness) asterisk-shaped Au nanostructures under the excitation of an incident pulse perpendicular to the *xy* plane with the electric field parallel to the *x*-axis. (a)-(c) Magnitude of the electric field normalized to the excitation field, E/E_0, as a function of the wavelength, at the points 1, 2, and 3 indicated in the insets to the corresponding right panels in each row. (d)-(f) Time evolution of the magnitude of the electric field at the points indicated in the inset to each panel.

To gain further insight into the effects of the lattice frustration regarding dipolar excitations of the nanoelements, we considered the time evolution of the optical response obtained from the simulation for the lattice with 500 nm / 50 nm / 45 nm / 30 nm (pitch / gap / width / thickness). Such analysis is worthwhile because Kagomé and other 2D hexagonal lattices exhibiting geometric magnetic frustration are well known in magnetism for showing slow relaxation of the magnetization associated with the evolution of the system through a complex energy landscape with a huge number of quasi-degenerate states [26,39–41]. Our work aims at exploring whether such a slow dynamics, caused by the interplay between localized and collective modes, may also emerge from the geometric frustration of interacting electric dipoles in plasmonic arrays with hexagonal symmetry, an approach that to our knowledge has not been reported yet. Figures 5(d)-5(f) show the time evolution of the magnitude of the electric field at the characteristic points of the lattice labeled 1, 2, and 3. Remarkably, the system remains active for over 70 fs after an excitation pulse of only about 8 fs long. The fact that the system resonates for such a long time makes these structures suitable for applications where the absorption and subsequent energy transfer of the exciting electromagnetic wave to another system should be maximized such as in enhanced Raman [1] and IR spectroscopies [5] or in photovoltaic applications [12]. Furthermore, the time evolution at the three feature points in Fig. 5 follows an oscillatory decay resulting from the convolution of some characteristic frequencies that modulate over time the swing of the system between the excitation modes. For instance, at points 1 and 2, the system alternates excitations corresponding to the LSR and SLR modes according to the E/E_0 distributions in Figs. 5(a) and 5(b). Thus, taking into account that at points 1 and 2, E/E_0 for the low-energy modes is significantly greater than for the high-energy modes, we can conclude that the higher peaks of the oscillating decay shown in Figs. 5(d) and 5(e) are associated with low-energy excitations of dipolar character (LSR modes). In fact, taking the time positions from the higher intensity peaks in Figs. 5(d) and 5(e) one retrieves a wavelength of 2350 and 2260 nm, respectively, in agreement with the NIR absorption peak. On the contrary, the time evolution at point 3 [Fig. 5(f)] is simpler since

Optics EXPRESS

predominant excitations at this point namely correspond to high-energy modes (SLR modes), as shown in the spectral distribution in Fig. 5(c). All the peaks of the oscillating decay are thus related to the excitation of SLR modes, in accordance with the frequency of the peaks in Fig. 5(f) that correspond to a wavelength of 788 nm, in agreement with the VIS absorption peak. The foregoing indicates that the extended time response of the array is due to the intricate interplay between local and collective plasmon modes, arising from the geometric frustration of interacting electric dipoles in lattices with hexagonal symmetry.

In order to shed further light on the swing of the system over time between the LSR and SLR excitation modes, Figure 6 shows some characteristic snapshots of the time evolution of $log(|E|^2/|E_0|^2)$ (see Visualization 1 and Visualization 2). Under excitation by a pulse perpendicular to the *xy* plane of the array with the electric field parallel to the *x*-axis, the optical response over time follows a complex oscillation through a wide range of modes. These modes expand from near-field configurations where the field is enhanced within the gaps along the *x*-axis and to a lesser extent within the tilted gaps (LSR modes; panels I-II), to collective modes where the FE is mostly confined inside the area occupied by each asterisk (for instance, in the V-shaped area between the bars conforming the asterisk) (SLR modes; panel V). Interestingly, at certain intermediate configurations (panels III-IV) most of the bare surface of the system exhibits a rather uniform FE distribution which may be of interest for some applications such as Surface Enhanced Raman Spectroscopy (SERS) and photovoltaic cells [1,12].

It is worth noting that lifetimes about 50 fs have already been reported in simpler lattices without frustration [21]. However, here we would like to emphasize that the way the system relaxes implies the echoed excitation of SLR modes at longer times than in other simpler lattices. This is especially noticeable in featured points 3 [Fig. 5(c) and 5(f)] where SLR modes are dominant over the whole time response of the system. Therefore, we show that geometric frustration improves the excitation of collective modes at relatively long times.

Finally, it should be highlighted that the FE in these plasmonic arrays extends over much larger areas than strongly coupled dimer antennas, with hotspots limited to the small gap in between the elements [14], and during much longer times than the excitation pulse [Fig. 5], thus making our structures interesting to increase the detection limit of biomolecules in enhanced Raman or fluorescence spectroscopies. Even though the maximum FE values (528 for the NIR peak and 268 for the VIS peak) are lower than those at the hotspots of bowtie antennas [14], our structures are prone to interact with a significantly larger density of target entities without the need of a precise positioning of the molecules. This would result in both an increase of the spectroscopic signal and a better reproducibility of the experiments, as compared to nanoantennas with highly confined hotspots which require a complicated positioning of the target molecules that limits the feasibility of the techniques [2].

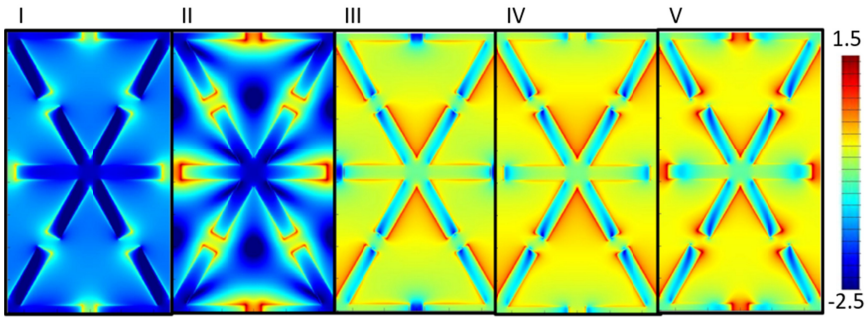

Fig. 6. Snapshots of the time evolution of $\log(|E|^2/|E_0|^2)$ for an array of 500 nm / 50 nm / 45 nm / 30 nm (pitch / gap / width / thickness) asterisk-shaped Au nanostructures recorded with increasing elapsed time following an incident excitation pulse perpendicular to the *xy* plane and with the electric field parallel to the x-axis (see Visualizations 1 and 2).

Optics EXPRESS

3. Conclusions

In summary, we have studied both numerically and experimentally the plasmonic response of arrays of Au nanoasterisks in a hexagonal lattice where neighboring elements are close enough to interact through near-fields and whose translational symmetry results in the excitation of collective modes. The inherent geometric frustration of dipolar polarizations in lattices with triangular symmetry destabilizes the low energy modes in favor of the collective ones yielding an expanded optical relaxation of the system through fluctuations between LSR and SLR modes. We conclude that this extended echoed excitation of SLR modes, which is still present at long times, is a consequence of the geometric frustration of the hexagonal lattice. Moreover, the use of the MIM configuration makes these systems perfect absorbers, a fact that is corroborated by FTIR experiments, with non-localized enhanced electric fields over large areas. Altogether, plasmonic nanostructures with geometrical frustration may be of interest as enhancers for spectroscopies such as Raman and fluorescence, magneto-plasmonics, non-linear optics or other applications that benefit from increased light absorption.

4. Appendix

4.1. Effect of light polarization

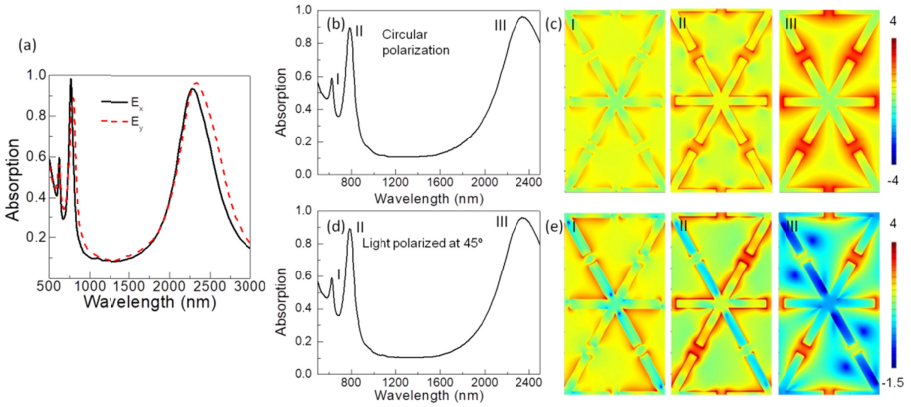

Fig. 7. Simulations of an array of 500 nm / 50 nm / 45 nm / 30 nm (pitch / gap / width / thickness) asterisk-shaped Au nanostructures, on a substrate with MIM configuration and a 100 nm-thick SiO_2 spacer layer. The source of light is incident perpendicular to the substrate. (a) Absorption spectra for two orthogonal polarizations of the incident electric field: i) along the *x*-axis, E_x, so that the electric field is parallel to one of the bars composing the asterisks (black solid line), and ii) along the *y*-axis (red dashed line), E_y. (b)-(c) Response under circular polarization: (b) absorption spectrum and (c) $Log(|E|^2/|E_0|^2)$ corresponding to the peaks I-III in (b). (d)-(e) Results for an excitation by light polarized at 45° with respect to *x*-axis: (d) absorption spectrum and (e) $Log(|E|^2/|E_0|^2)$ corresponding to the peaks I-III in (d).

Previous studies showed the dependence of the coupling between light and plasmonic nanostructures on the polarization of the incident pulse [17]. Therefore, in order to compare FTIR results to those of the simulations, it must be considered that experimental measurements are usually collected with unpolarized light, while simulations are carried out with the electric field of the excitation source parallel to one of the coordinate axis. Thus, to characterize the response of the system under unpolarized light, two simulations with orthogonal polarizations (along *x* and *y* axes) are performed. However, Fig. 7(a) shows that no significant differences are present in the absorption of our system between the two polarization axes, so it is assumed that the results obtained by FTIR and FDTD simulations shown in the main text can be directly compared to each other. Results for light with circular polarization and light polarized at 45° with respect to the horizontal gap are also presented [Fig. 7(b)-7(e)], showing only slight modifications in the absorption spectra.

Optics EXPRESS

4.2. Discrepancies between FTIR measurements and simulations

Although simulations and experimental results are in qualitative agreement, there are still some differences between them, especially regarding the width of the peak in the visible. First of all, simulations have been performed with nanostructures having a 30 nm thick Au layer to achieve almost perfect absorption in the visible. However, due to lift-off problems, these nanostructures are troublesome to fabricate. Instead, a Au thickness of 20 nm has been used in the manufactured samples. This obviously has some effects on the plasmonic response, which are shown in Fig. 8(a). Even though the percentage of absorbed light in the visible is decreased, it remains over 94% for Au thicknesses comprised between 20 and 40 nm, which provides flexibility to the nanofabrication procedure. Nevertheless, the Au thickness affects dramatically the absorption in the IR region, which is notably reduced for 40 nm Au thick nanostructures. Besides, simulations show that, for a Cr adhesion layer of 5 nm, the two peaks in the visible are notably broadened and start to collapse in a single one [Fig. 8(b)], making the spectra more similar to the FTIR results [Fig. 3]. Even though in our case the adhesion layer is not as thick, we expect to find broader experimental peaks that the simulated ones due to several effects such as imperfections, a non-continuous adhesion layer, granularity etc.

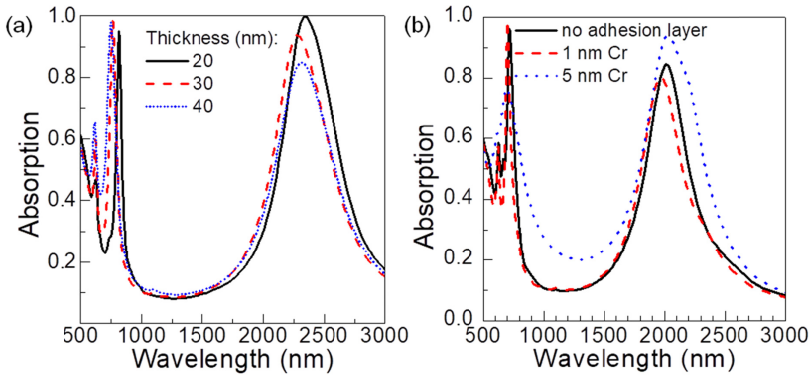

Fig. 8. Simulated absorption spectra of an array of asterisks of 500 nm / 50 nm / 45 nm (pitch / gap / width) on top of a substrate with MIM configuration and being the spacer a 100 nm thick SiO_2 layer, (a) as a function of Au thickness; (b) for a Au thickness of 30 nm and several Cr thicknesses.

Moreover, samples show slight variations on the geometrical parameters of the nanoelements throughout the array that may also alter their local optical response. Then, the recorded experimental signal in a macroscopic area is actually an average over the local geometries of the array. In order to gain insight on the effect of this geometrical variability, Fig. 9 shows the optical response of free standing asterisk arrays as a function of some parameters. We can observe that by keeping the gap constant and increasing the pitch of the array and the length of the bars, both peaks redshift. However, when the pitch is kept constant (as during EBL), the peak in the visible barely changes, while the NIR peak shifts towards longer wavelengths for decreasing gap width. It is also worth noting that even though both absorption peaks are present for all the cases studied, the addition of the MIM configuration to the substrate produces a huge increase in their intensities (see Fig. 4 as an example).

Optics EXPRESS

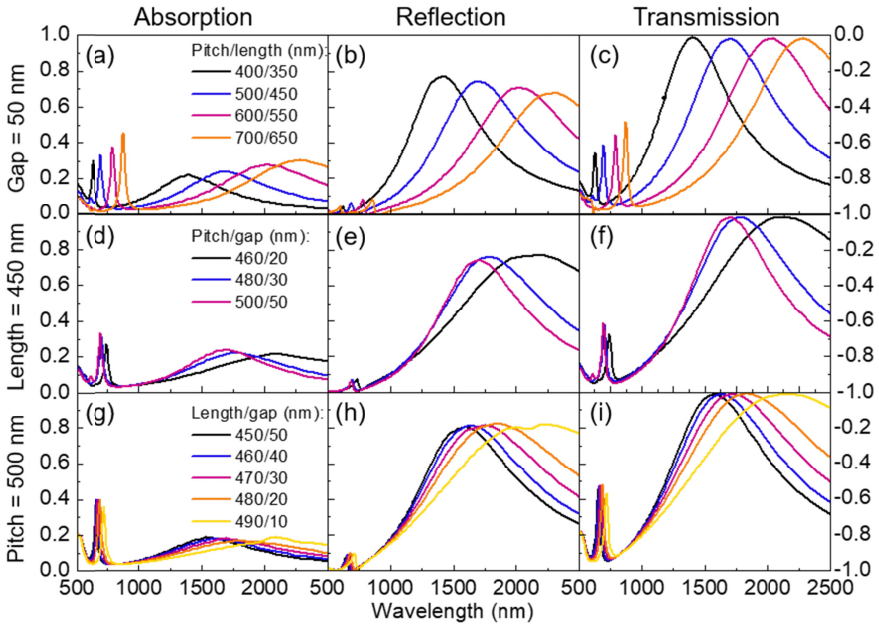

Fig. 9. Absorption, reflection and transmission FDTD simulated curves for several array geometries. No substrate has been used for these simulations in order to study the effect of the geometry of the array only.

As shown before by the simulations, the two absorption peaks suffer a redshift with decreasing gap width. If we analyze the actual gap distributions in the real samples from SEM images [Fig. 2(b) and 2(c)], the experimental broadening of the peaks (shown in Fig. 3) could be partially accounted for by averaging the absorption curves for different gap sizes [Fig. 10(b) and 10(d) top panels] accordingly to the percentage of gaps of each size in the real sample [Fig. 10(a) and 10(c)].

Another contribution to the discrepancies between FTIR measurements and simulations may come from the fact that some real nanoelements rather look like a central dot of a finite diameter with bars emerging from it [Fig. 2] than being the ideal asterisk-shaped nanoelements used in the simulations. To account for this, several simulations have been performed with nanoelements with modified geometries according to the real samples for an array of asterisks of 500 nm, 50 nm, 30 nm, 0.5 nm Cr + 30 nm Au (pitch, gap, width, thickness) [Fig. 11]. To begin with, corners of the EBL-fabricated structures tend to be rounded. To account for this, a cylinder with a diameter equal to the thickness of the bar was added to the end of the bars forming the asterisks, whose length was reduce by a length equal to the radius of the cylinder, keeping constant the width of the gap [Fig. 11(a)]. Besides, the nanoelements are not purely rectangular bars overlapped like those shown in the FDTD design, but they rather have a bigger center as compared to the end of the bars. This is due to an overexposure of the center as compared to the ends of the bars. To compensate for this, a central cylinder of 200 nm was added at the center of the asterisk [Fig. 11(b)]. When adding that central cylinder, the intersection between two bars makes a rounded outwards form, while in the fabricated samples this rounded shape is inwards. To account for that inwards shape in the simulations, a cylinder etch of 66 nm in diameter was added to obtain this effect [Fig. 11(c)]. Finally, taking into account the AFM profiles (not shown), semi-spheres were added at the ends of the stars.

Optics EXPRESS

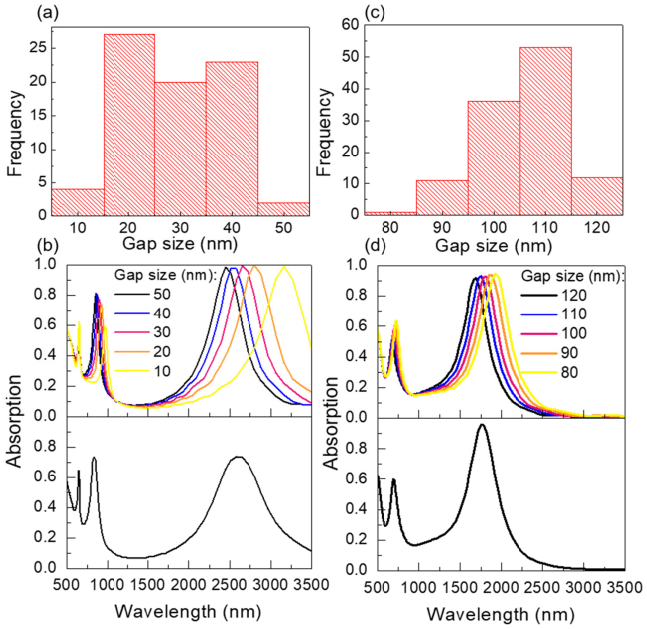

Fig. 10. Effect of the gap distribution in the absorption spectra for two asterisk arrays with pitch of 400 nm (a)-(b) and pitch of 500 nm (c)- (d), respectively, both metallized with 0.5 nm Cr + 20 nm Au and fabricated on a substrate with MIM configuration, being the spacer layer 100 nm of SiO_2. (a) and (c) show the gap distributions obtained from the SEM images in Fig. 2(b) and 2(c), and correspond to the measurements shown in Fig. 3. Top (b) and (d) panels show the absorption spectra as a function of the gap size, while bottom panels show the resulting averaged curves according to the distributions in (a) and (c) panels, respectively.

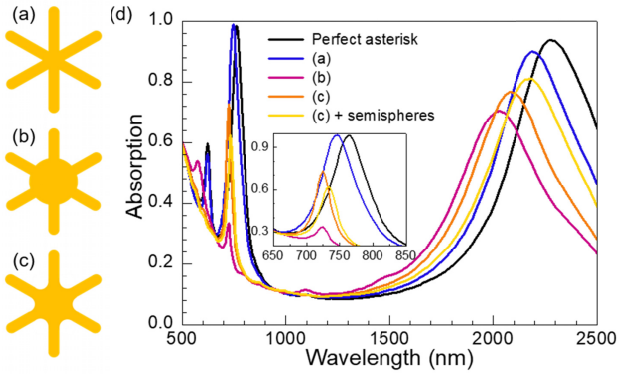

Fig. 11. Effect of shape correction in the absorption spectrum. (a)-(c) Schemes of the simulated samples with different corrections of the shape: (a) asterisk with the rounded shape correction of the bars' ends. (b) correction in (a), plus an added 200 nm in diameter central cylinder to account for overexposure in the central part. (c) corrections in (b) plus inwards rounded junctions between bars and the central cylinder. (d) Absorption spectra for the different corrections sketched in (a)-(c) and semispheres placed at the ends of the bars.

Funding

Spanish MINECO (MAT2015-68772- P, BES-2013-065377); Spanish ICTS Network MICRONANOFABS, partially supported by MINECO; European Union FEDER funds (Una manera de hacer Europa).

Optics EXPRESS

Acknowledgment

We thank R. Pérez for the electron beam evaporation and Dr. A. Espinha and Dr A. Mihi for the FTIR measurements.

Disclosures

The authors declare that there are no conflicts of interest related to this article.

References

1. L. Du, X. Zhang, T. Mei, and X. Yuan, "Localized surface plasmons, surface plasmon polaritons, and their coupling in 2D metallic array for SERS," Opt. Express **18**(3), 1959–1965 (2010).
2. A. Rakovich, P. Albella, and S. A. Maier, "Plasmonic Control of Radiative Properties of Semiconductor Quantum Dots Coupled to Plasmonic Ring Cavities," ACS Nano **9**(3), 2648–2658 (2015).
3. M. Baia, L. Baia, S. Astilean, and J. Popp, "Surface-enhanced Raman scattering efficiency of truncated tetrahedral Ag nanoparticle arrays mediated by electromagnetic couplings," Appl. Phys. Lett. **88**(14), 143121 (2006).
4. L. V. Brown, X. Yang, K. Zhao, B. Y. Zheng, P. Nordlander, and N. J. Halas, "Fan-Shaped Gold Nanoantennas above Reflective Substrates for Surface-Enhanced Infrared Absorption (SEIRA)," Nano Lett. **15**(2), 1272–1280 (2015).
5. F. Neubrech, C. Huck, K. Weber, A. Pucci, and H. Giessen, "Surface-Enhanced Infrared Spectroscopy Using Resonant Nanoantennas," Chem. Rev. **117**(7), 5110–5145 (2017).
6. Z. H. Jiang, S. Yun, F. Toor, D. H. Werner, and T. S. Mayer, "Conformal Dual-Band Near-Perfectly Absorbing Mid-Infrared Metamaterial Coating," ACS Nano **5**(6), 4641–4647 (2011).
7. R. Alaee, "Optical Nanoantennas and Their Use as Perfect Absorbers," Karlsruher Institut für Technologie (KIT) (2015).
8. F. Liu, X. Zhang, and X. Fang, "Plasmonic plano-semi-cylindrical nanocavities with high-efficiency local-field confinement," Sci. Rep. **7**(1), 40071 (2017).
9. T. K. Hakala, H. T. Rekola, A. I. Väkeväinen, J.-P. Martikainen, M. Nečada, A. J. Moilanen, and P. Törmä, "Lasing in dark and bright modes of a finite-sized plasmonic lattice," Nat. Commun. **8**, 13687 (2017).
10. M. Kuttge, F. J. García de Abajo, and A. Polman, "Ultrasmall Mode Volume Plasmonic Nanodisk Resonators," Nano Lett. **10**(5), 1537–1541 (2010).
11. W. Zhou, M. Dridi, J. Y. Suh, C. H. Kim, D. T. Co, M. R. Wasielewski, G. C. Schatz, and T. W. Odom, "Lasing action in strongly coupled plasmonic nanocavity arrays," Nat. Nanotechnol. **8**(7), 506–511 (2013).
12. H. A. Atwater and A. Polman, "Plasmonics for improved photovoltaic devices," Nat. Mater. **9**(3), 205–213 (2010).
13. S. Gottheim, H. Zhang, A. O. Govorov, and N. J. Halas, "Fractal nanoparticle plasmonics: The cayley tree," ACS Nano **9**(3), 3284–3292 (2015).
14. L. Lin and Y. Zheng, "Optimizing plasmonic nanoantennas via coordinated multiple coupling," Sci. Rep. **5**, 14788 (2015).
15. A. D. Humphrey, N. Meinzer, T. A. Starkey, and W. L. Barnes, "Surface Lattice Resonances in Plasmonic Arrays of Asymmetric Disc Dimers," ACS Photonics **3**(4), 634–639 (2016).
16. S. Bagheri, K. Weber, T. Gissibl, T. Weiss, F. Neubrech, and H. Giessen, "Fabrication of Square-Centimeter Plasmonic Nanoantenna Arrays by Femtosecond Direct Laser Writing Lithography: Effects of Collective Excitations on SEIRA Enhancement," ACS Photonics **2**(6), 779–786 (2015).
17. R. Guo, T. K. Hakala, and P. Törmä, "Geometry dependence of surface lattice resonances in plasmonic nanoparticle arrays," Phys. Rev. B **95**(15), 155423 (2017).
18. Y. Chen, J. Dai, M. Yan, and M. Qiu, "Metal-insulator-metal plasmonic absorbers: influence of lattice," Opt. Express **22**(25), 30807–30814 (2014).
19. A. D. Humphrey and W. L. Barnes, "Plasmonic surface lattice resonances on arrays of different lattice symmetry," Phys. Rev. B **90**(7), 075404 (2014).
20. Y. Chen, J. Dai, M. Yan, and M. Qiu, "Honeycomb-lattice plasmonic absorbers at NIR: anomalous high-order resonance," Opt. Express **21**(18), 20873–20879 (2013).
21. B. Auguié and W. L. Barnes, "Collective Resonances in Gold Nanoparticle Arrays," Phys. Rev. Lett. **101**(14), 143902 (2008).
22. Y. Chu, E. Schonbrun, T. Yang, and K. B. Crozier, "Experimental observation of narrow surface plasmon resonances in gold nanoparticle arrays," Appl. Phys. Lett. **93**(18), 181108 (2008).
23. S. Pourjamal, M. Kataja, N. Maccaferri, P. Vavassori, and S. van Dijken, "Hybrid Ni/SiO2/Au dimer arrays for high-resolution refractive index sensing," Nanophotonics **7**(5), 905–912 (2018).
24. M. J. Huttunen, P. Rasekh, R. W. Boyd, and K. Dolgaleva, "Using surface lattice resonances to engineer nonlinear optical processes in metal nanoparticle arrays," Phys. Rev. A **97**(5), 053817 (2018).
25. L. Michaeli, S. Keren-Zur, O. Avayu, H. Suchowski, and T. Ellenbogen, "Nonlinear Surface Lattice Resonance in Plasmonic Nanoparticle Arrays," Phys. Rev. Lett. **118**(24), 243904 (2017).
26. A. Farhan, P. M. Derlet, A. Kleibert, A. Balan, R. V. Chopdekar, M. Wyss, L. Anghinolfi, F. Nolting, and L. J. Heyderman, "Exploring hyper-cubic energy landscapes in thermally active finite artificial spin-ice systems," Nat. Phys. **9**(6), 375–382 (2013).
27. S. R. Giblin, S. T. Bramwell, P. C. W. Holdsworth, D. Prabhakaran, and I. Terry, "Creation and measurement of long-lived magnetic monopole currents in spin ice," Nat. Phys. **7**(3), 252–258 (2011).
28. G. Weick, C. Woollacott, W. L. Barnes, O. Hess, and E. Mariani, "Dirac-like Plasmons in Honeycomb Lattices of Metallic Nanoparticles," Phys. Rev. Lett. **110**(10), 106801 (2013).

Optics EXPRESS

29. N. Maccaferri, L. Bergamini, M. Pancaldi, M. K. Schmidt, M. Kataja, S. Dijken, N. Zabala, J. Aizpurua, and P. Vavassori, "Anisotropic Nanoantenna-Based Magnetoplasmonic Crystals for Highly Enhanced and Tunable Magneto-Optical Activity," Nano Lett. **16**(4), 2533–2542 (2016).
30. M. Kataja, S. Pourjamal, N. Maccaferri, P. Vavassori, T. K. Hakala, M. J. Huttunen, P. Törmä, and S. van Dijken, "Hybrid plasmonic lattices with tunable magneto-optical activity," Opt. Express **24**(4), 3652–3662 (2016).
31. M. Kataja, T. K. Hakala, A. Julku, M. J. Huttunen, S. van Dijken, and P. Törmä, "Surface lattice resonances and magneto-optical response in magnetic nanoparticle arrays," Nat. Commun. **6**(1), 7072 (2015).
32. A. P. Ramirez, "Geometric frustration: Magic moments," Nature **421**(6922), 483 (2003).
33. W. W. Salisbury, "Absorbent body for electromagnetic waves," U.S. patent US2599944 A (1943).
34. Lumerical Solutions Home Page (n.d.).
35. E. D. Palik, *Handbook of Optical Constants of Solids* (Academic, 1985), **1**.
36. P. B. Johnson, R. W. Christy, and R. C. P. B. Johnson, "Optical Constants of Noble Metal," Phys. Rev. B **6**(12), 4370–4379 (1972).
37. F. Colas, D. Barchiesi, S. Kessentini, T. Toury, and M. L. de la Chapelle, "Comparison of adhesion layers of gold on silicate glasses for SERS detection," J. Opt. **17**(11), 114010 (2015).
38. T. G. Habteyes, S. Dhuey, E. Wood, D. Gargas, S. Cabrini, P. J. Schuck, A. P. Alivisatos, and S. R. Leone, "Metallic Adhesion Layer Induced Plasmon Damping and Molecular Linker as a Nondamping Alternative," ACS Nano **6**(6), 5702–5709 (2012).
39. J. P. Morgan, A. Stein, S. Langridge, and C. H. Marrows, "Thermal ground-state ordering and elementary excitations in artificial magnetic square ice," Nat. Phys. **7**(1), 75–79 (2011).
40. V. Kapaklis, U. B. Arnalds, A. Farhan, R. V. Chopdekar, A. Balan, A. Scholl, L. J. Heyderman, and B. Hjörvarsson, "Thermal fluctuations in artificial spin ice," Nat. Nanotechnol. **9**(7), 514–519 (2014).
41. A. Farhan, P. M. Derlet, A. Kleibert, A. Balan, R. V. Chopdekar, M. Wyss, J. Perron, A. Scholl, F. Nolting, and L. J. Heyderman, "Direct Observation of Thermal Relaxation in Artificial Spin Ice," Phys. Rev. Lett. **111**(5), 057204 (2013).